

SOLAR CELLS

Cation reactivity inhibits perovskite degradation in efficient and stable solar modules

Yong Ding^{1,2†}, Bin Ding^{2,3†}, Pengju Shi^{4†}, Jan Romano-deGea^{2†}, Yahui Li^{4†}, Roland C. Turnell-Ritson², Olga A. Syzgantseva⁵, Ilhan Yavuz⁶, Ming Xia⁴, Ruohan Yu⁷, Maria A. Syzgantseva⁸, Jean-Nicolas Audinot⁹, Xiaohe Miao⁴, Xiaobin Liao⁷, Jiantao Li¹⁰, Patrick Dörflinger¹¹, Vladimir Dyakonov¹¹, Cheng Liu¹, Yi Yang¹, Li Tao¹², Keith G. Brooks², Andre Slonopas¹³, Jiahong Pan¹⁴, Lei Zhang⁷, Qinyou An⁷, Yaoguang Rong⁷, Jun Peng³, Liming Ding¹⁵, Enzheng Shi⁴, Liqiang Mai⁷, Songyuan Dai¹, Kangning Zhao^{2,7*}, Jiang Sheng^{16*}, Rui Wang^{4*}, Paul J. Dyson^{2*}, Mohammad Khaja Nazeeruddin^{2*}

Perovskite solar modules (PSMs) show outstanding power conversion efficiencies (PCEs), but long-term operational stability remains problematic. We show that incorporating *N,N*-dimethylmethyleniminium chloride into the perovskite precursor solution formed dimethylammonium cation and that previously unobserved methyl tetrahydrotriazinium ($[MTTZ]^+$) cation effectively improved perovskite film. The *in situ* formation of $[MTTZ]^+$ cation increased the formation energy of iodine vacancies and enhanced the migration energy barrier of iodide and cesium ions, which suppressed nonradiative recombination, thermal decomposition, and phase segregation processes. The optimized PSMs achieved a record (certified) PCE of 23.2% with an aperture area of 27.2 cm², with a stabilized PCE of 23.0%. The encapsulated PSM retained 87.0% of its initial PCE after ~1900 hours of maximum power point tracking at 85°C and 85% relative humidity under 1.0-sun illumination.

High efficiency and long-term stability are essential requirements for commercial perovskite solar modules (PSMs) (1, 2). Despite recent improvements in the power conversion efficiencies (PCEs) of PSMs, the degradation caused by extrinsic factors such as moisture, heat, and light irradiation need to be resolved (3–5). In particular, thermal- and light-induced phase degradation of three-dimensional (3D) perovskites ABX₃ (where A and B are cations at their respective sites and X is typically a halide anion) limit the stability of PSMs (6, 7).

Considerable advances have been achieved by the addition of ionic-liquid additives (8, 9) and Lewis acid-base dopants (10–12), as well as the use of surface passivation strategies (13, 14). However, these advancements have not yet fulfilled the minimum stability criteria for commercial application. A Lewis-basic ionic-liquid additive, 1,3-bis(cyanomethyl)imidazolium chloride ([Bcmim]Cl), was previously used in our work to inhibit the degradation of the perovskite precursor solution and promote the homogeneous phase of the perovskite films (9), but the [Bcmim]⁺ cation cannot dope into the perovskite lattice and so fails to suppress the perovskite degradation under thermal stress (fig. S1). Thus, to

further enhance the stability of PSMs, a comprehensive strategy is needed in combination with fundamental stability-enhancing mechanisms.

Here, we describe the addition of *N,N*-dimethylmethyleniminium chloride ([Dmei]Cl) into perovskite precursor solutions to produce two cations *in situ*—namely 3-methyl-2,3,4,5-tetrahydro-1,3,5-triazin-1-ium ($[MTTZ]^+$) and dimethylammonium ($[DMA]^+$) cations (Fig. 1A)—that enhanced the photovoltaic (PV) performance and stability of PSMs. The PSMs that were prepared delivered a certified PCE of 23.2% on an aperture area of 27.2 cm². The encapsulated PSM exhibited long-term stability, with a linear extrapolation to a T₉₀ (time to 10% loss of PCE) exceeding 8000 hours under the ISOS-L-1 stability protocol (ISOS, International Summit on Organic Photovoltaic Stability), where the conditions are 25°C with maximum power point (MPP) tracking and a relative humidity (RH) of ~30% under 1.0-sun illumination, and an extrapolated T₈₀ (time to 20% loss of PCE) exceeding 4000 hours at 85°C with MPP tracking, 85% RH, under 1.0-sun illumination. The underlying mechanism for these enhancements caused by the presence of the *in situ* formed cations is also discussed.

Reactivity between the [Dmei]Cl additive and the A cations

The [Dmei]⁺ cation was chosen for this study because it is comparable in size to the guanidinium ($[Gua]^+$) cation but is oppositely and asymmetrically polarized, as revealed by the electrostatic potential (ESP) profiles and steric radii of the [Dmei]⁺ and [Gua]⁺ cations (fig. S2). Additional benefits of the [Dmei]⁺ cation were increased film quality and PV performance (figs. S3 to S7 and supplementary text). Within minutes of introducing [Dmei]Cl to the perovskite precursor solution (PPS) containing MAI, FAI, CsCl, MACl, and PbI₂ (MAI, methylammonium iodide; FAI, formamidinium iodide; CsCl, cesium chloride; PbI₂, lead iodide), the expected signals of the [Dmei]⁺ cation at 3.6 parts per million (ppm) and 8.2 ppm were no longer visible in the ¹H nuclear magnetic resonance (NMR) spectrum. Instead, four new signals were observed, including three corresponding ¹³C{¹H} NMR peaks (fig. S8, A and B). The NMR spectra, together with ¹H–¹³C heteronuclear single-quantum coherence (HSQC) and heteronuclear multiple-bond correlation (HMBC) spectra, showed that a previously unreported cationic species, $[MTTZ]^+$, selectively formed *in situ* (Fig. 1A and fig. S8, C and D).

Further evidence for the existence of the $[MTTZ]^+$ cation within the films was obtained by solid-state NMR spectroscopy (ssNMR). In the ¹H ssNMR spectrum, a peak at 4.9 ppm was observed only for the film doped with [Dmei]Cl (fig. S9). This peak corresponded to the CH₂ protons of the cation (4.2 ppm in the solution phase ¹H NMR spectra; fig. S8A). Only ternary combinations of [Dmei]Cl, FAI, and MAI yielded the $[MTTZ]^+$ cation, confirming that both the FA⁺ and MA⁺ cations were required to react with [Dmei]⁺ to produce the $[MTTZ]^+$ cation (fig. S10), with the concomitant formation of the $[DMA]^+$ cation and the release of HX (X is Cl or I) (Fig. 1A). This hypothesis was supported by the observation of the $[DMA]^+$ cation by ¹H and ¹³C{¹H} NMR spectroscopy (fig. S8, A and B, and fig. S11) and by the sharpening of the relevant proton peaks in the ¹H NMR spectrum of PPS upon addition of [Dmei]Cl (fig. S9B).

When mixing [Dmei]Cl in a 1:1 ratio with either FAI or MAI, the $[MTTZ]^+$ cation was not observed (fig. S10). Because of the chemical equilibrium and the thermodynamics of the reaction, we could not isolate pure salts of the $[MTTZ]^+$ cation from the mixture. However,

¹Beijing Key Laboratory of Novel Thin-Film Solar Cells, North China Electric Power University, 102206 Beijing, China. ²Institut des Sciences et Ingénierie Chimiques, Ecole Polytechnique Fédérale de Lausanne (EPFL), CH-1015 Lausanne, Switzerland. ³College of Chemistry, Chemical Engineering and Materials Science, Soochow University, 215123 Suzhou, China. ⁴School of Engineering, Westlake University, 310024 Hangzhou, China. ⁵Department of Chemistry, Lomonosov Moscow State University, 119991 Moscow, Russia. ⁶Department of Physics, Marmara University, 34722 Istanbul, Türkiye. ⁷State Key Laboratory of Advanced Technology for Materials Synthesis and Processing, Wuhan University of Technology, 430070 Wuhan, China. ⁸Department of Physics, Mendeleev University of Chemical Technology, Moscow 125047, Russia. ⁹Advanced Instrumentation for Nano-Analytics (AINA), Materials Research and Technology Department, Luxembourg Institute of Science and Technology (LIST), L-4422 Belvaux, Luxembourg. ¹⁰Chemical Sciences and Engineering Division, Argonne National Laboratory, Lemont, IL, 60439 USA. ¹¹Experimental Physics VI, University of Würzburg, 97074 Würzburg, Germany. ¹²School of Microelectronics, HuBei University, 430062 Wuhan, China. ¹³Whiting School of Engineering, Department of Materials Science and Engineering, Johns Hopkins University, Baltimore, MD 21218, USA. ¹⁴State Key Laboratory of Featured Metal Materials and Life-Cycle Safety for Composite Structures, School of Resources, Environment and Materials, Guangxi University, 530004 Nanning, China. ¹⁵National Center for Nanoscience and Technology, Chinese Academy of Sciences, 100190 Beijing, China. ¹⁶ChangZhou S.C. Exact Equipment Co., 213002 Changzhou, China.

*Corresponding author. Email: yicyle@126.com (K.Z.); shengjiang@chinasc.com.cn (J.S.); wangrui@westlake.edu.cn (R.W.); paul.dyson@epfl.ch (P.J.D.); mdkhaja.nazeeruddin@epfl.ch (M.K.N.)

†These authors contributed equally to this work.

we attempted to grow perovskite single crystals from the PPS containing FAI, MAI, [Dmei]I, and PbI₂ and successfully obtained 1D [DMA]PbI₃ and [MTTZ]PbI₃ single crystals that we analyzed with single-crystal x-ray diffraction (SC-

XRD) (fig. S12 and table S1). Two different polymorphs of the single crystals of [MTTZ]PbI₃ were identified. One, a lower symmetry, metastable polymorph, was recorded at higher temperature (80°C) and upon cooling to room

temperature became a higher-symmetry polymorph with a similar structure (fig. S12).

The photoluminescence (PL) spectrum of the [Dmei]Cl film exhibited a dominant emission peak at ~792 nm and weak emission peaks at

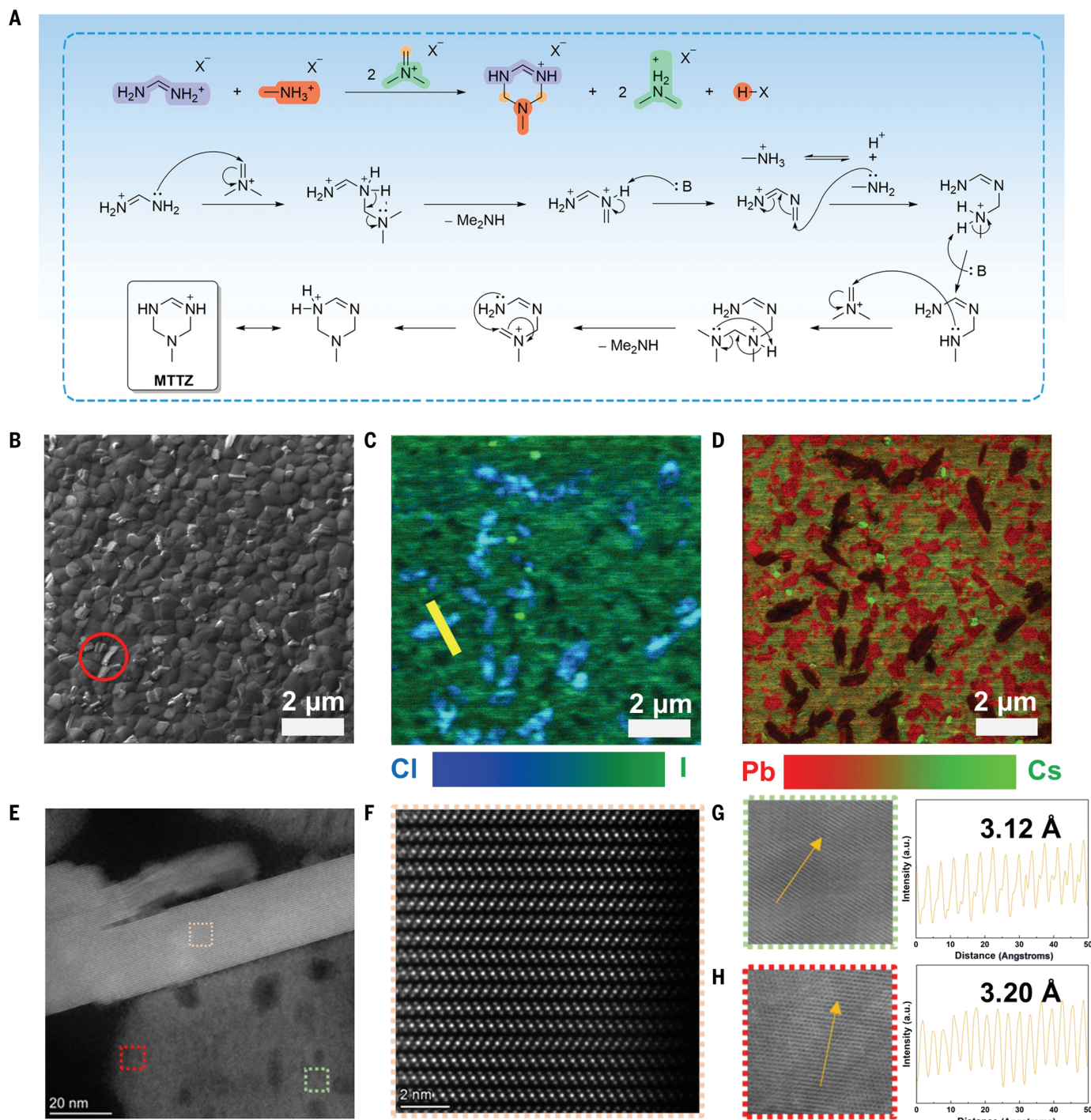


Fig. 1. Reaction mechanism, morphology, elemental mapping, and crystal lattice of the [Dmei]Cl perovskite films. (A) Proposed mechanism for the *in situ* formation of the $[\text{MTTZ}]^+$ and $[\text{DMA}]^+$ cations. (B) Secondary electron image of the [Dmei]Cl film obtained using HIM. The red circle highlights 1D grains. (C) HIM-SIMS elemental mapping of ^{35}Cl in blue and ^{127}I in cyan. (D) Overlap elemental mapping of ^{133}Cs in green and ^{208}Pb in red. (E) High-resolution

transmission electron microscopy (TEM) image of the [Dmei]Cl film. (F) Expansion of the pink dashed square in (E) corresponding to 1D perovskite. (G) Expansion of the green dashed square in (E) corresponding to 3D perovskite in the bulk region (left), and the corresponding interplanar spacing (right). (H) Expansion of the red dashed square in (E) corresponding to 3D perovskite in the edge region (left), and the corresponding interplanar spacing (right).

~530, 590, and 625 nm (fig. S13). The stable $[MTTZ]PbI_3$ single crystal displayed an emission peak at ~610 nm, whereas the metastable $[MTTZ]PbI_3$ single crystal showed emission peaks at ~540, 580, and 625 nm. In addition, an emission peak at ~700 nm was observed in the single crystal of $[DMA]PbI_3$. It appears that the 1D perovskites containing the $[MTTZ]^+$ and $[DMA]^+$ cations existed simultaneously in the $[Dmei]Cl$ film.

Characterization of the perovskite films

The optimal concentration of $[Dmei]Cl$ in the perovskite, based on the formula $Cs_{0.05}MA_{0.05}FA_{0.9}PbI_3$, was 1.0 mol % (termed “[$Dmei]Cl$ ”; fig. S4). The time-of-flight–secondary ion mass spectrometry (TOF-SIMS) depth profiles of the $[Dmei]Cl$ film revealed that the $[DMA]^+$ and $[MTTZ]^+$ cations were highly concentrated on the surface of the perovskite film, with some fraction distributed within the bulk perovskite (fig. S14). In addition, the helium ion microscopy–SIMS (HIM-SIMS) image demonstrated that the $[Dmei]Cl$ film had a compact morphology with a 1D rod structure distributed mainly on the surface (Fig. 1B, highlighted by the red circle), unlike the granular grains of the perovskite film without $[Dmei]Cl$ (termed “control”; fig. S15).

In negative ion mode, the ^{14}N signal showed almost the same intensity in all regions, but strong enrichment in the ^{35}Cl and ^{127}I signals from the 1D grains was observed (Fig. 1C and fig. S16, A and B). Similarly, in positive ion mode, a distinct depletion of the ^{133}Cs signal was observed and the ^{208}Pb signal showed both higher- and lower-intensity variations over the same region (Fig. 1D). The line scan in the Pb–Cs map revealed depletion of the Cs signal and enrichment of Pb signal across the 1D grains (fig. S16C), suggesting that the 1D grains were composed of Pb, N, Cl, and I, which is consistent with elemental components of $[MTTZ]PbCl_xI_{3-x}$ and $[DMA]PbCl_xI_{3-x}$ (15, 16).

The precise structure of the perovskite films was further elucidated by the high-angle annular dark field (HAADF) scanning transmission electron microscopy (STEM) micrography of the bulk perovskite particles, where the intensity is sensitive to the atomic number (Z). The panoramic view revealed the coexistence of rod-shaped particles and bulk phase (Fig. 1E), which agrees with the HIM-SIMS (Fig. 1B). The coexistence of Cl, I, N, and Pb was observed in both the rod structures and bulk phase, as revealed in the STEM mapping in fig. S17. The rod-like structure presented a distinct 1D perovskite structure with large and small bright protrusions, corresponding to Pb and I atoms (Fig. 1F), respectively. Furthermore, the layer spacing of the 3D perovskite increased from the bulk region (3.12 Å; Fig. 1G) to the edge area (3.20 Å; Fig. 1H), further confirming that the larger cations were incorporated into the

surface region of 3D perovskite lattice (17, 18). In addition, energy-dispersive spectroscopy (EDS) (as shown in fig. S17) indicated that both the $[MTTZ]^+$ and $[DMA]^+$ cations were mostly present in the 1D perovskite, whereas the $[MTTZ]^+$ and $[DMA]^+$ cations were doped in the A sites at the surface of the perovskite lattice, with the EDS data indicating that the dopant level of $[MTTZ]^+$ and $[DMA]^+$ was <6 at % (table S2 and supplementary text).

Measurements by x-ray photoelectron spectroscopy (XPS) reveal a shift of N 1s peak from 400.9 to 400.8 eV and the appearance of a new N 1s peak at ~397.9 eV, indicative of the formation of 1D $[MTTZ]PbCl_xI_{3-x}$ and $[DMA]PbCl_xI_{3-x}$ (fig. S18), because the N 1s peak at 400.8 eV may be assigned to the NH_2^+ group in the $[DMA]^+$ cation (19), whereas the new N 1s peak at 397.9 eV could be ascribed to the NH^+ group in the $[MTTZ]^+$ cation. (20) In addition to the two prominent Pb 4f peaks (143.7 eV for $4f_{5/2}$ and 138.8 eV for $4f_{7/2}$), which could be ascribed to the lead perovskite structure, the control film exhibited two lower intensity peaks at 141.9 and 137.1 eV, indicative of metallic Pb (Pb^0) (21). However, Pb 4f XPS spectra of the $[Dmei]Cl$ film displayed only the perovskite peaks, suggesting that the in situ-formed $[MTTZ]^+$ and $[DMA]^+$ cations prevented the reduction of lead to metallic Pb.

The optical gap of the $[Dmei]Cl$ film was slightly higher than that of the control film, as evidenced from the ultraviolet-visible (UV-Vis) absorption spectra (fig. S19). In addition, time-resolved microwave conductivity measurements showed that the charge carrier mobility, average free-carrier lifetime and charge carrier diffusion length (L_d) of the $[Dmei]Cl$ film were dramatically enhanced (fig. S20 and table S3) (22). This change reflected the slower decay of the $[Dmei]Cl$ film, determined from the femtosecond-transient absorption spectra (fig. S21A and table S3). The prolonged lifetime of the $[Dmei]Cl$ film indicated less charge recombination in both the bulk and surface states, evidenced by reduced defects from space-charge-limited current (SCLC) model (fig. S21B) (23). Conductive atomic force microscopy (c-AFM) images show that the fresh $[Dmei]Cl$ film has higher conductivity than the fresh control film (Fig. 2, A and B), suggesting that incorporating $[Dmei]Cl$ into the perovskite could facilitate charge transport, reduce defects, and suppress nonradiative recombination (24).

Thermal stability of the perovskite films

c-AFM enabled in situ observation of thermally induced perovskite degradation at 85°C. The local conductivity of the control film decreased overall, and the dark regions grew (Fig. 2A and fig. S22A), suggesting that the thermal aging process led to degradation into PbI_2 (25). However, the conductivity of the $[Dmei]Cl$ film increased after 1 hour and maintained identical

conductivity throughout the heating process that lasted for 2 hours (Fig. 2B and fig. S22B), which was consistent with the evolution of peak intensities of the perovskite phase from XRD patterns. As shown in fig. S22C, the peak intensity of the control film decreased to ~50% of its initial state after 600 hours, whereas appreciable degradation of the $[Dmei]Cl$ film was not observed. The decomposition of the control film led to a slight red shift of the UV-Vis absorption spectrum after thermal aging (fig. S22D) (26).

The chemical environment of Pb in the perovskite films was probed by using atomic pair distribution function (PDF) analysis, which indicated that the Pb–I bond length increases from 3.14 Å in the control film to 3.17 Å in the $[Dmei]Cl$ film (Fig. 2C). We attributed this change to the larger size of the $[MTTZ]^+$ and $[DMA]^+$ cations compared with that of the FA^+ cation, which is consistent with the STEM analysis (Fig. 1, G and H) and the calculated average Pb–I distances (table S4) (27, 28). The intensity of the Pb–I peaks in both samples was similar, suggesting that incorporating the $[MTTZ]^+$ and $[DMA]^+$ cations did not perturb the short-range order of the perovskite and avoids local defects. In addition, extended x-ray absorption fine structure (EXAFS) analysis of the control and $[Dmei]Cl$ films showed identical absorption-edge energies before and after aging (Fig. 2D), confirming that the oxidation state of Pb in the perovskite films is +2.

Detailed structural information of the control and $[Dmei]Cl$ films was obtained from k^2 -weighted EXAFS fitting analysis and the corresponding Fourier transform of k -space EXAFS (R-space) shown in Fig. 2, E and F. The R-space EXAFS spectra showed peaks at ~2.2 Å for Pb–O bonds and ~2.8 Å for Pb–I bonds (29, 30). The Pb–I bond length of 3.14 Å for the control film and 3.17 Å for the $[Dmei]Cl$ film were deduced from fitting these peaks (Fig. 2G), which is in agreement with the corresponding distances obtained from the PDF data.

The mean-square relative displacement of absorber and backscatter atoms, σ^2 , corresponded to 0.015 Å² in the control film and 0.010 Å² in the $[Dmei]Cl$ film, suggesting a slight improvement in the short-range order in the $[Dmei]Cl$ film and indicating enhanced structural stability. Moreover, the coordination number of the Pb^{2+} ions in the $[Dmei]Cl$ film approached 6 (Fig. 2H), indicating that the Pb^{2+} ion was electronically saturated, meaning that it had fewer defects in the perovskite layer, which is beneficial for maintaining efficient charge separation kinetics (31). After thermal aging, the coordination number of the Pb^{2+} ion in the control film is reduced from 7.2 to 4.7 (Fig. 2H), which could be attributed to the formation of a PbI_2 phase (32). In comparison, the coordination number in the $[Dmei]Cl$ film was 5.9, near the original value (Fig. 2H), suggesting that the

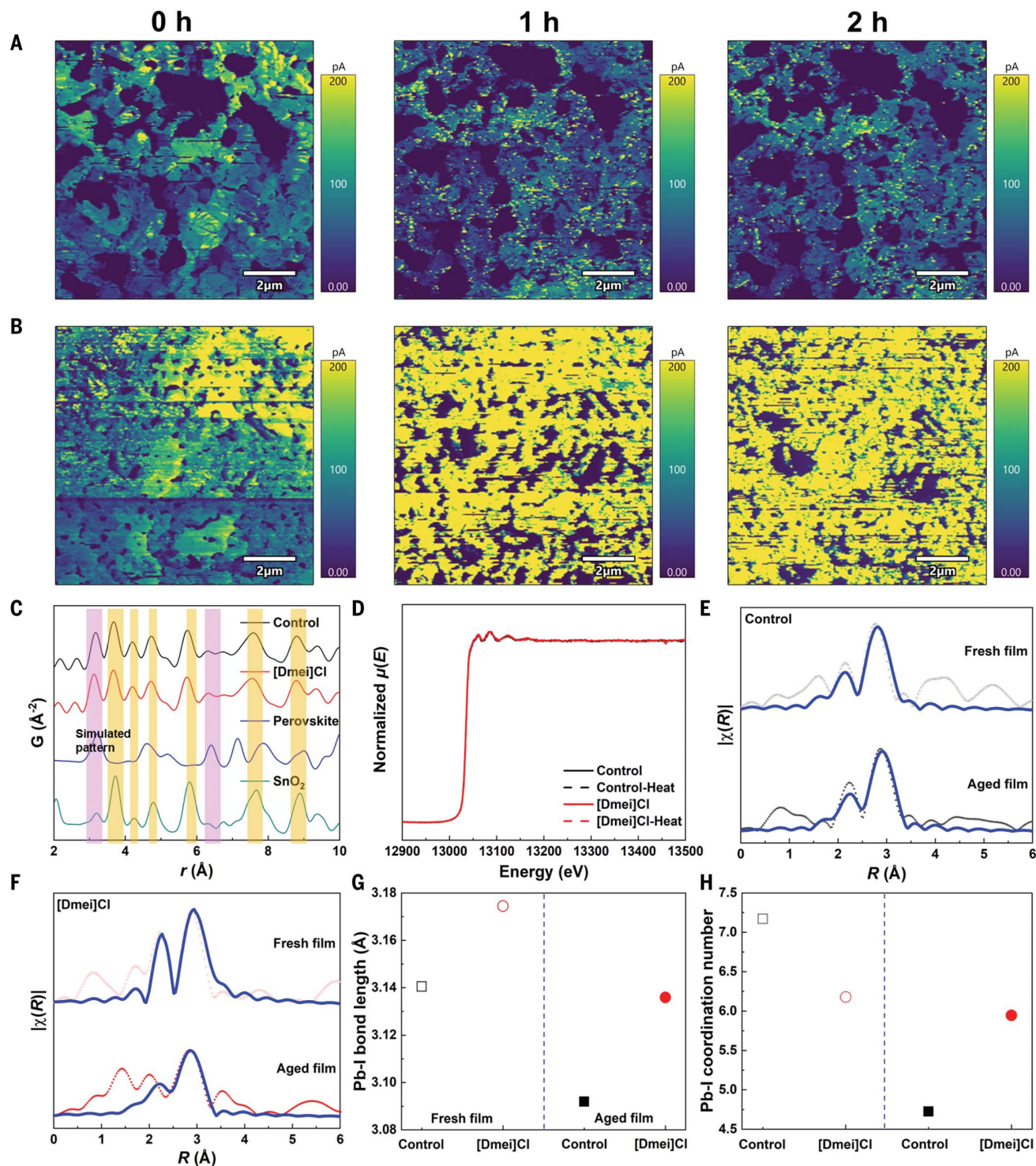


Fig. 2. In situ conductivity and local crystal structure of the perovskite films during thermal aging. The evolution of c-AFM maps at different heating intervals for the (A) control and (B) [Dmei]Cl films. (C) Comparison between experimental and calculated differential PDF spectra of fresh perovskite films. The contribution of the perovskite and SnO_2 phases is highlighted in pink and orange, respectively, according to the simulation pattern of SnO_2 and $\text{Cs}_{0.05}\text{MA}_{0.05}\text{FA}_{0.9}\text{PbI}_3$ perovskite. (D) Normalized Pb L_{III} edge x-ray absorption

coefficient [$\mu(E)$] for the control and [Dmei]Cl films without and with thermal aging at 100°C for 24 hours. XAS spectra and fitting in R-space for (E) the control film before and after aging, and (F) the [Dmei]Cl film before and after aging. The dashed lines represent the experimentally determined data, and the solid blue lines correspond to simulated data. (G) The simulated Pb–I bond lengths and (H) Pb–I coordination numbers of the control and [Dmei]Cl films before and after aging.

[Dmei]Cl film maintained a stable perovskite structure with fewer vacancies and was less susceptible to thermal degradation (27).

Light-soaking stability of the perovskite films

Light-induced degradation was probed by local PL imaging of the perovskite films. We tracked PL peak positions and intensities during 8 hours of concentrated light illumination equivalent to 4.5 suns (Fig. 3). After continuous light soaking for 2 hours, the PL peak intensity of the control film increased and its position shifted to a slightly wider bandgap (Fig. 3A), which we attributed to a reduction in surface defects under illumination (33). After 6 hours of illumination, the emergence of localized wide band-

gap (narrow bandgap) regions was observed, corresponding to Cs⁺-rich (and hence FA⁺-poor) domains (Fig. 3C) (34). The number of these domains grew with time, and cation segregation occurred on the perovskite surface after 8 hours of continuous illumination. The PL from the [Dmei]Cl film also increased in intensity (Fig. 3B), but the [Dmei]Cl film displayed a more homogeneous distribution, and cation segregation was not observed (Fig. 3D), suggesting that incorporating the [MTTZ]⁺ and [DMA]⁺ cations into the perovskite inhibited phase segregation under continuous light illumination.

Grazing incidence x-ray diffraction (GIXRD) experiments were performed to investigate the depth-dependent strain distribution in perov-

skite films. A shift in diffraction peak to higher diffraction angle (2θ) was found in both the control and [Dmei]Cl films as penetration depth increased (figs. S23, A and B). However, the effect was considerably more pronounced for the [Dmei]Cl film, in which the strain was calculated to be 85.1 MPa, compared with 49.1 MPa for the control film (fig. S23C), indicating that incorporating the [MTTZ]⁺ and [DMA]⁺ cations provided a minor compressive strain in the perovskites, stabilizing the perovskite lattice and increasing the activation energy (E_a) of ion migration (35, 36). The E_a was evaluated by using temperature- and time-dependent photocurrent measurements (fig. S23D) (37). The E_a was estimated to be 350 and 610 meV

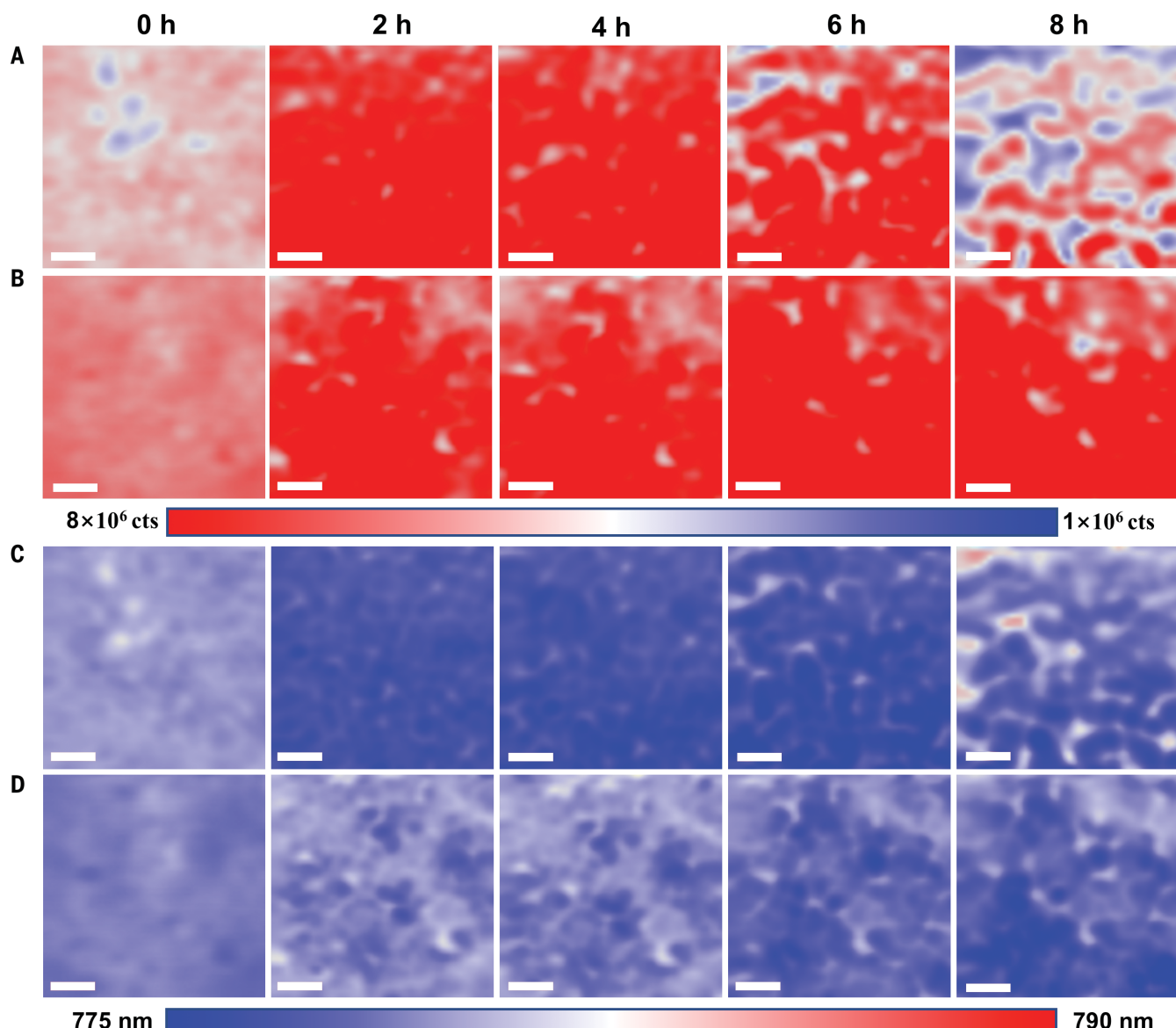


Fig. 3. Light stress on the PL peak intensity and position of the perovskite films. In situ PL intensity maps on the same region of the (A) control and (B) [Dmei]Cl films over time under white-light illumination with an intensity of 450 mW cm^{-2} (equivalent to 4.5 suns). The corresponding PL peak position of the (C) control and (D) [Dmei]Cl films. Scale bars, $2 \mu\text{m}$.

for the control and [Dmei]Cl devices, respectively, confirming the suppression of ion migration in the [Dmei]Cl devices. Decreased ion migration may be attributed to the reduced iodine vacancies (V_I) and the higher energy

barrier of iodine and cesium ions to ion migration by the synergistic effect of the $[DMA]^+$ and $[MTTZ]^+$ cations.

We predicted the formation energies of V_I using density functional theory (DFT) (fig. S24).

The control perovskite had a stable neutral V_I defect throughout the majority of the bandgap region and exhibited a charge transition level at ~0.3 eV, indicating the presence of potentially deep charge traps for charge carrier

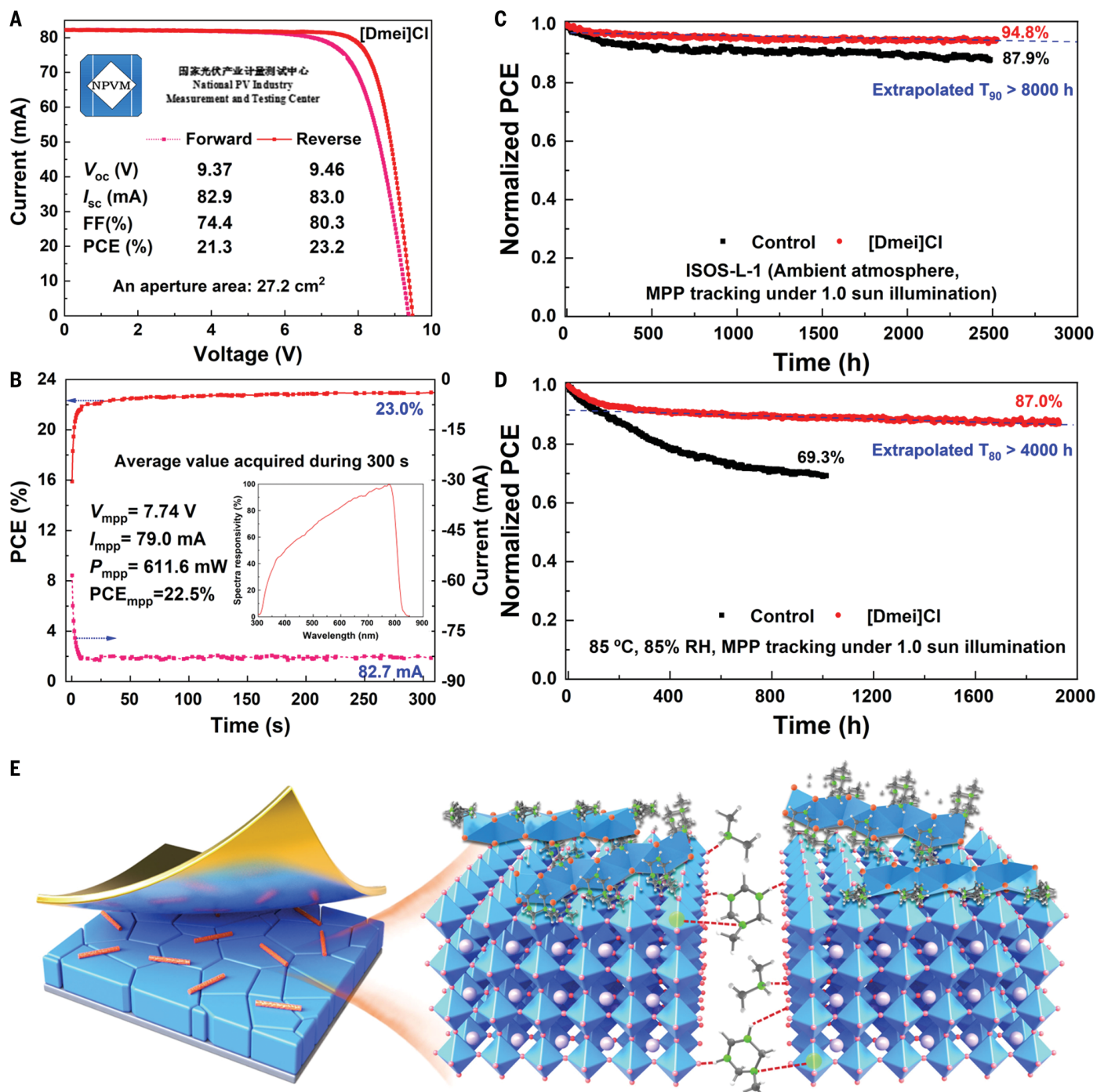


Fig. 4. PV performance and long-term operational stability of PSMs. (A) The certified current-voltage (I - V) curves from forward and reverse scans of a [Dmei]Cl PSM with an aperture area of 27.2 cm² from NPVM, China. (B) The certified stabilized efficiency of a [Dmei]Cl PSM. The inset in (B) is the relative spectral responsivity curve. (C) ISOS-L-1 stability protocols of the encapsulated PSMs measured under MPP tracking and continuous light irradiation with a white light-emitting diode (LED) lamp. (D) The encapsulated PSMs measured under MPP tracking and continuous light irradiation with a white LED lamp, 100 mW·cm⁻² at 85°C and 85% RH. The initial PCE of the control and [Dmei]Cl PSMs are 21.3 and 23.2%, respectively. (E) Schematic showing the roles of $[MTTZ]^+$ and $[DMA]^+$ in the 3D perovskite matrix.

100 mW·cm⁻² under ambient conditions. The initial PCE of the control and [Dmei]Cl PSMs are 21.3 and 23.1%, respectively. (D) The encapsulated PSMs measured under MPP tracking and continuous light irradiation with a white LED lamp, 100 mW·cm⁻² at 85°C and 85% RH. The initial PCE of the control and [Dmei]Cl PSMs are 21.3 and 23.2%, respectively. (E) Schematic showing the roles of $[MTTZ]^+$ and $[DMA]^+$ in the 3D perovskite matrix.

recombination. In addition, the formation energy of the V_I defect in the control perovskite at the valence-band maximum state was 2.3 eV, versus 2.9 eV for the perovskite with the $[DMA]^+$ and $[MTTZ]^+$ cations (fig. S25), demonstrating the suppression of the formation of V_I in the perovskite. Furthermore, the perovskite with the $[MTTZ]^+$ cation contributed to inhibiting the formation of V_I in the perovskite with the $[DMA]^+$ cation (figs. S25 and S26).

The energy barrier for an I^- ion migrating to a V_I is ~370 meV (38). The presence of the $[MTTZ]^+$ cation increased the energy barrier to 783 meV, with a slight reduction for the $[DMA]^+$ cation (361 meV; fig. S27). In addition, the energy barrier for the Cs^+ ion migration increased from 420 meV of the control perovskite to 525 and 602 meV after doping with the $[DMA]^+$ and $[MTTZ]^+$ cations, respectively (fig. S28). The increased energy barriers of ion migration could be attributed to the ability of the $[MTTZ]^+$ and $[DMA]^+$ cations to form extensive hydrogen bonds with I^- ions, as well as the valence states of the Cs^+ ions, which is apparent from the simulations of the Cs^+ ion migration pathway (19, 38). Because ions migrated faster at grain boundaries and interfaces than within the bulk perovskite (39), the $[DMA]^+$ and $[MTTZ]^+$ cations distributed at the surface and the grain boundaries inhibited the I^- and Cs^+ ion migration at grain boundaries and interfaces, which slowed down phase segregation under illumination.

PV performance and stability of PSMs

We fabricated PSMs composed of eight subcells connected in series with a geometrical fill factor (GFF) of 96.5%. The $[Dmei]Cl$ PSMs achieved a PCE of 23.3%, along with an open-circuit voltage (V_{oc}) of 9.33 V and fill factor (FF) of 80.9%, on an aperture area of 29.0 cm^2 (fig. S29). The PCE for the control PSMs was 22.0%. Furthermore, the PV performance of the PSMs was reproducible (fig. S30), with average PCEs of 21.4% for the control PSMs and 23.0% for the $[Dmei]Cl$ PSMs.

The $[Dmei]Cl$ PSMs were sent to the National PV Industry Measurement and Testing Center (NPVM), China, for certification. The efficiencies of reverse and forward scans on an aperture area of 27.2 cm^2 were 23.2% and 21.3%, respectively (Fig. 4A), and each subcell with an aperture area of 3.4 cm^2 had a V_{oc} of 1.19 V and FF of 80.5%, suggesting remarkably reduced nonradiative recombination losses in the $[Dmei]Cl$ PSMs. The stabilized power output under MPP tracking of the $[Dmei]Cl$ PSM was 23.0% (Fig. 4B), with an average stabilized PCE of 22.5% (fig. S31), which was the highest stabilized efficiency for reported PSMs to date (table S5).

We used two protocols to determine the long-term operational stability of the PSMs. Under ISOS-L-1 conditions, the encapsulated $[Dmei]Cl$ PSM showed only 5.2% relative PCE loss after

2500 hours of continuous operational testing, whereas the PCE of the control PSM decreased by 12.1% (Fig. 4C). We used T_{90} to evaluate the operational lifetime. The T_{90} of the control PSM was ~1830 hours, whereas the $[Dmei]Cl$ PSM had a much higher T_{90} of ≥ 8000 hours. Furthermore, the $[Dmei]Cl$ PSM maintained 87.0% of its initial PCE over 1900 hours at 85°C with MPP tracking, 85% RH, under 1.0-sun illumination, and the T_{80} lifetime was estimated to be 4000 hours. The control PSM decreased to 69.3% of its initial PCE after 1200 hours and had a much lower T_{80} value of only 250 hours (Fig. 4D).

Identifying the origin of improved efficiency and stability

Because the isolation of the $[MTTZ]^+$ cation has not been achieved owing to the dynamic equilibrium of the reaction, the ball-milling product containing both the $[MTTZ]^+$ and $[DMA]^+$ cations that we used to prepare the 1D single crystals was also used to elucidate the impact of the cations in the perovskites. We introduced 1.0 mol% of the mixture into the PPS to fabricate perovskite films and devices (termed “ $[MTTZ]^+/[DMA]^+$ ”). In addition, 1.0 mol % of the commercial $[DMAI]$ salt was also doped into PPS for comparison (termed “ $[DMA]^+$ ”). The PV metrics shown in figs. S32A and S33 demonstrated that the improvement in PCE of the $[Dmei]Cl$ device originated from the $[MTTZ]^+$ cation, which could dramatically increase the crystallinity and PL intensity of the perovskite films, as evidenced by XRD patterns (fig. S32B), PL spectra, and time-resolved photoluminescence decay (fig. S32, C and D), and spatially resolved lifetime mappings (fig. S34). However, the $[DMA]^+$ cation has a negative impact on the film quality and device performance, which is consistent with the reduced formation energy of V_I defects (figs. S25 and S26).

An in situ thermal degradation XRD analysis confirmed that the control film gradually increased the intensity of PbI_2 diffraction peaks but showed that the $[Dmei]Cl$ film retained the unchanged intensity of PbI_2 peaks (fig. S35). Similarly, the film containing $[MTTZ]^+/[DMA]^+$ exhibited a modest increase in the intensity of PbI_2 peaks. By contrast, the $[DMA]^+$ film degraded at a faster rate than the control film, indicating that the perovskite with the $[DMA]^+$ cation was detrimental to the thermal stability of the perovskite films. On the basis of the above analysis, the improved PV performance and stability of the $[Dmei]Cl$ devices could be attributed to the $[MTTZ]^+$ cation (18). The $[MTTZ]^+$ cation, located at the grain boundaries, was incorporated into the perovskite surface, such that the $-NH$ groups formed hydrogen bonds with iodide in multiple spatial directions, increasing the formation energy of V_I defects (40). Additionally, the methyl-bound N atom had a lone pair of electrons capable of coordinating

with Pb^{2+} ions, thereby enhancing the stabilization of the perovskites (fig. 4E) (41). Together, these factors contributed to the mitigation of perovskite degradation under thermal and light stress.

Discussion

The $[Dmei]^+$ cation reacted with MA^+ and FA^+ cations in the perovskite precursor solution to generate the $[DMA]^+$ and $[MTTZ]^+$ cations. The $[MTTZ]^+$ cation stabilized the resulting perovskite structures and increased the migration barrier energies of I^- and Cs^+ ions, thus inhibiting perovskite degradation and phase segregation. In addition, the $[MTTZ]^+$ cation increased the formation energy of iodine vacancy and improved film crystallinity, leading to reduction of nonradiative recombination loss and enhancement of charge transport, which affords a record PCE of 23.2% combined with exceptional high stability.

REFERENCES AND NOTES

- Z. Liu et al., *Nat. Energy* **5**, 596–604 (2020).
- T. Bu et al., *Nat. Energy* **7**, 528–536 (2022).
- S. Sidhik et al., *Science* **377**, 1425–1430 (2022).
- Y. Zhao et al., *Nat. Mater.* **21**, 1396–1402 (2022).
- A. D. Jodłowski et al., *Nat. Energy* **2**, 972–979 (2017).
- S. He, L. Qiu, L. K. Ono, Y. Qi, *Mater. Sci. Eng. Rep.* **140**, 100545 (2020).
- D. B. Khadka, Y. Shirai, M. Yanagida, K. Uto, K. Miyano, *Sol. Energy Mater. Sol. Cells* **246**, 111899 (2022).
- Y.-H. Lin et al., *Science* **369**, 96–102 (2020).
- B. Ding et al., *Nature* **628**, 299–305 (2024).
- R. Wang et al., *Science* **366**, 1509–1513 (2019).
- S. You et al., *Science* **379**, 288–294 (2023).
- C. Li et al., *Science* **379**, 690–694 (2023).
- R. Azmi et al., *Science* **376**, 73–77 (2022).
- S. M. Park et al., *Science* **381**, 209–215 (2023).
- O. J. Usiobio et al., *J. Phys. Chem. C Nanomater. Interfaces* **124**, 23230–23236 (2020).
- Y. Zhao et al., *Science* **377**, 531–534 (2022).
- D. P. McMeekin et al., *Nat. Mater.* **22**, 73–83 (2023).
- E. A. Duijnsteet et al., *J. Am. Chem. Soc.* **145**, 10275–10284 (2023).
- S. Tan et al., *Adv. Mater.* **32**, e1906995 (2020).
- Y. Zhu et al., *J. Mater. Chem. A Mater. Energy Sustain.* **5**, 9272–9278 (2017).
- L. Wang et al., *Science* **363**, 265–270 (2019).
- F. Zhang et al., *Science* **375**, 71–76 (2022).
- H. Li, J. Lu, T. Zhang, Y. Shen, M. Wang, *ACS Energy Lett.* **3**, 1815–1823 (2018).
- C. M. M. Soe et al., *J. Am. Chem. Soc.* **139**, 16297–16309 (2017).
- G. Zheng et al., *Nat. Commun.* **9**, 2793 (2018).
- A. A. Sutanto et al., *Nano Lett.* **20**, 3992–3998 (2020).
- I. Spanopoulos et al., *J. Am. Chem. Soc.* **143**, 7069–7080 (2021).
- Y. Fu, *Adv. Mater.* **34**, e2108556 (2022).
- D.-H. Kang, Y.-J. Park, Y.-S. Jeon, N.-G. Park, *J. Energy Chem.* **67**, 549–554 (2022).
- C. Ma et al., *Science* **379**, 173–178 (2023).
- J. A. McLeod, Z. Wu, B. Sun, L. Liu, *Nanoscale* **8**, 6361–6368 (2016).
- Z. Ni et al., *Nat. Energy* **7**, 65–73 (2021).
- Z. Andaji-Garmaroudi et al., *Adv. Mater.* **31**, e1902374 (2019).
- Y. Bai et al., *Science* **378**, 747–754 (2022).
- C. Zhu et al., *Nat. Commun.* **10**, 815 (2019).
- D. Liu et al., *Nat. Mater.* **20**, 1337–1346 (2021).
- C. Barnes et al., *Nat. Commun.* **6**, 7497 (2015).
- S. Tan et al., *Nature* **605**, 268–273 (2022).
- Z. Zhang et al., *Adv. Mater.* **36**, e2313860 (2024).
- E. Ugur et al., *Science* **385**, 533–538 (2024).
- H. Wei, Y. Yang, S. Chen, H. J. Xiang, *Nat. Commun.* **12**, 637 (2021).

ACKNOWLEDGMENTS

The Valais Energy Demonstrators fund supported this work. We also thank the US Department of Energy (DOE), Office of Energy Efficiency and Renewable Energy, Vehicle Technologies Office. This research used resources of the Advanced Photon Source (beamlines 11-ID-C and 12-BM), a US DOE Office of Science User Facility, operated for the DOE Office of Science by Argonne National Laboratory under contract no. DE-AC02-06CH11357. We thank S. Lee and T. Li for providing technical support. We thank the shared research facilities of HPC computing resources at Lomonosov Moscow State University. We thank L. Piveteau and the NMR spectroscopy platform at EPFL for support with solid-state NMR spectroscopy measurements. In addition, we thank K. Zhao at Shaanxi Normal University for trying to synthesize single crystals and D. Savary for assisting with the structural elucidation.

Funding: We thank the Swiss National Science Foundation (SNSF) and Luxembourg Fonds National de la Recherche (FNR, "SUNSPOT," grant no. 11244141), SNSF, for the financial support of the SOLAR4D project, SNSF project no. 200020L_1729/1 and FNR INTER no. 16/11534230. V.D. and P.D. acknowledge financial support by the Deutsche Forschungsgemeinschaft (DFG) in the frame of the Priority Program SPP 2196 (project DY 18/14-1). This work was supported by the European Union's Horizon 2020 program, through a FET Proactive research and innovation action under grant agreement no. 101084124 (DIAMOND), and by the 111 Project (B16016), the Project of Scientific and Technological Support Program in Jiang Su Province (BE2022026-2), and the Natural Science Foundation of Hubei Province (no. 2022CFB402). E.S. acknowledges financial support from the Research Center

for Industries of the Future at Westlake University, National Natural Science Foundation of China (grant no.52272164). R.W. acknowledges the grant (LD24E02001) from the Natural Science Foundation of Zhejiang Province of China. Part of the computing sources used in this work were provided by the National Center for High Performance Computing (UHEM) of Türkiye. The authors also thank École Polytechnique Fédérale de Lausanne, which provided additional financial support. **Author contributions:** Y.D., B.D., and P.J.S. designed and supervised the research as well as the performance of efficient small-size devices and large-area PSMs. P.J.S. performed the AFM, c-AFM, *in situ* PL mapping, and XRD measurements with supervision from R.W., J.R.-deG., and R.C.T.-R. L.T. performed the solution and solid-state NMR spectroscopy measurements and analysis. R.Y. performed STEM measurements with supervision from K.N.Z. J.T.L performed the PDF and XAFS characterization with supervision from K.N.Z. and O.A.S. M.A.S. conducted the DFT calculations. X.H.M. performed *in situ* XRD measurements. I.Y. performed DFT simulations of ion migration and calculated the defect formation energy. X.L. made DFT simulations of ESP with supervision of L.Q.M. J.-N.A. conducted the ambient HIM-SIMS and TOF-SIMS characterization. J.P. fabricated compact TiO₂ layers using the physical vapor deposition method. J.S. performed long-term stability measurements. J.H.P. performed transient absorption spectroscopy. Y.H.L. and M.X. fabricated single crystals and analyzed with supervision from E.Z.S. P.D. performed the TRMC characterization with supervision from V.D. C.L. and Y.Y. conducted XPS and SCLC measurements. L.Z. and Y.G.R. performed the measurements of activation energy and GIXRD with supervision from Q.Y.A. Y.D. and B.D. wrote the first draft of the manuscript, and

all authors contributed feedback and comments. A.S., K.N.Z., J.S., L.M.D., S.Y.D., R.W., P.J.S., and M.K.N. directed and supervised the research. **Competing interests:** The authors declare that they have no competing interests. **Data and materials availability:**

All data needed to evaluate the conclusions are present in the paper or the supplementary materials. The accession numbers for the crystal structure .cif files reported in this manuscript were CCDC 2308544 ([Dmei]PbCl_{0.41}I_{0.59}), CCDC 2308545 ([Dmei]PbI₃), CCDC 2308547 ([DMA]PbI₃), CCDC 2308548 (metastable [MTTZ] PbI₃), and CCDC 2308549 ([MTTZ]PbI₃), which were deposited at the Cambridge Crystallographic Data Centre. **License information:**

Copyright © 2024 the authors, some rights reserved; exclusive licensee American Association for the Advancement of Science. No claim to original US government works. <https://www.science.org/about/science-licenses-journal-article-reuse>

SUPPLEMENTARY MATERIALS

science.org/doi/10.1126/science.ado6619

Materials and Methods

Supplementary Text

Figs. S1 to S35

Tables S1 to S6

References (42–67)

Submitted 18 March 2024; resubmitted 5 July 2024

Accepted 1 October 2024

10.1126/science.ado6619